Nonlinear response in a Weyl semimetal

Shi Feng

Abstract

Weyl semimetals have attracted considerable attention in the last decade in quantum condensed matter physics, due to their unique topological band structure characterized by robust Weyl nodes, and their possible applications to electronics. Recently, the study of Weyl semimetals have been extended to their optical properties, especially through the measurements of non-linear responses. In this paper, I present (i) the fundamental aspects of Weyl semimetals, including their basic notion, topological signatures, and discussions on symmetry. (ii) non-linear second harmonic (SH) optical effects in Weyl semimetals, in the sense that the response of the material to the applied field depends quadratically on the field amplitude and that the output frequency is twice the input frequency. By using an effective Floquet two band model, I present that such second harmonic generation (SHG) in Weyl semimetals is intimately related to the Berry connection of the two Floquet bands, and is characterized by a giant anisotropic susceptibility with a universal $\chi^{(2)} \propto 1/\omega$ scaling which is reported by the experiment by Wu *et al* [1].

CONTENTS

I. INTRODUCTION

Recently, many theoretical and experimental endeavors have been devoted to the physical realization/probe of new classes of materials, such as topological insulators and semimetals, with the latter been a 3D analog of the former. A topological insulator has an energy gap in the bulk, however, unlike traditional insulators or semiconductors, topological insulators are topologically non-trivial insulators characterized by topological quantum numbers. A fundamental consequence and principle experimental indicator of the non-trivial topology is one or more robust metallic (gapless) surface states that are protected both from localization and backscattering by time-reversal symmetry.

In semimetals, Dirac- or Weyl-like band crossings appear in momentum space and is protected by discrete symmetries. Topological semimetals has attracted great interest since they host quasi-particles, like Weyl/Dirac fermions, that cannot occur in vacuum but do occur in solid-state systems. Being a 3D analog of 2D topological insulators, lots of properties of the latter can be mapped to semimetals, e.g. Fermi arcs in semimetals can be viewed a bundle of surface edge states in topological insulators. Nevertheless, unlike a topological insulator, the band crossings in semimetals are robust and cannot be gapped out by perturbations due to the 3D nature of Weyl equation (the existence of band crossing is guaranteed by 3 independent ks. Perturbing the 3D Hamiltonian with a mass term merely moves the location of band crossing in the momentum space; hence the corresponding 3D systems are termed semimetals).

The robust band-crossings, termed Weyl nodes or Weyl points, have many usually non-trivial topological features from which interesting physics emerges. In this paper, I am going to focus on the experimental phenomenon and theoretical model of non-linear optical generation in Weyl semimetals. This paper is organized as follows. Section II introduces the theory of Weyl semimetals, including some of their basic notions and unique characteristics. Section III introduces the fundamental aspects of non-linear optical effects with an emphasis on the second harmonic generation, where I will discuss the mechanism of (Second harmonic) non-linear response in terms of a Floquet band model. Section III presents results of a recent experiment on Weyl material that shows a giant anisotropic optical response, followed by a quantitative discussion using the Floquet formalism discussed in section II.

II. THEORY OF WEYL SEMIMETALS

This section introduces the notion of Weyl semimetal as a transition from Dirac equation and Dirac semimetal. Dirac semimetals can be viewed as a 3D analog of graphene at K, K' points where low energy excitation can be effectively described by (pseudo-) Dirac equation. Dirac semimetal is an intermediate phase of matter between normal metals and normal insulators. On the one hand, the nature of 3D massless Dirac Hamiltonian guarantees the existence of zero band gap or gapless modes; one the other hand, its conduction and valence band touch only at discrete points, which are termed Dirac nodes, at which the band gap vanishes leading to the property of a semi-metal. In the following subsection, I discuss the generic Dirac equation, and present how Weyl equation, thus Weyl semimetals, is derived thereafter.

A. Dirac Equation

For simplicity, in the following all are assumed in 3+1 dimension, with speed of light in natural units $c = 1$, or in solids $v_F = 1$. Dirac nodes can be described by the four-component Dirac spinors $\psi(x^\mu)$ which satisfies the famous Dirac equation

$$(i\gamma^\mu \partial_\mu - m)\, \psi(x^\mu) = 0 \tag{1}$$

where $\mu = 0, 1, 2, 3$ which label the time and space dimensions, and the 4 γ matrices with the anti-commutator:

$$\{\gamma^\mu, \gamma^\nu\} = 2g^{\mu\nu} \tag{2}$$

where $g^{\mu\nu}$ is the metric tensor. This gives the anti-commutation relation $\{\gamma^\mu, \gamma^\nu\} = 0$ for $\mu \neq \nu$ and $(\gamma^0)^2 = 1$, $(\gamma^1)^2 = (\gamma^2)^2 = (\gamma^3)^2 = -1$. This yields the following Dirac representation

$$\gamma^0 = \begin{pmatrix} \mathbb{1}_{2\times 2} & 0 \\ 0 & -\mathbb{1}_{2\times 2} \end{pmatrix}, \quad \gamma^i = \begin{pmatrix} 0 & \sigma^i \\ -\sigma^i & 0 \end{pmatrix} \tag{3}$$

where σ^i are 2×2 pauli matrices. This yelds eigen energy solutions $E_\pm = \pm\sqrt{p^2 + m^2}$, thus the minimal band gap is twice the mass $|m|$, and conduction and valance bands corresponds to the positive and negetive energy states. The band gap vanishes if $m = 0$ and the excitation becomes massless at the band crossing point, termed Dirac point, where m changes its sign.

The topological stability of Dirac points is protected by time reveral symmetry $\mathcal{T}$ and parity symmetry $\mathcal{P}$. When $\mathcal{T}$ is respected, Kramers theorem says $\epsilon_n(\vec{k}) = \epsilon_{n'}(-\vec{k})$, which forms a Kramers pair of bands, and we have 2-fold degeneracy at TRIM. Furthermore, if $\mathcal{P}$ symmetry is present, the parity transformaion $\vec{k} \to -\vec{k}$ gives $\epsilon_{n'}(\vec{k}) = \epsilon_{n'}(-\vec{k})$. Comparing with the Kramers pairs of bands we have $\epsilon_n(\vec{k}) = \epsilon_{n'}(\vec{k})$. Hence we conclude that the two Kramers bands are degenerate at *all* momenta, which gives doubly degenerate bands. This, as will be clear soon and in next subsectoin, gives the 4-fold degeneracy of Dirac node.

To have a better understanding of this band crossing, let us look at the parity of wavefunction. The $\mathcal{P}$ transformation of a Dirac particle is:

$$\mathcal{P}\psi(\vec{x}) = \gamma^0 \psi(-\vec{x}) \tag{4}$$

Note this is different from non-relativistic particle where the parity transformation is $\mathcal{P}\psi(\vec{x}) = \psi(-\vec{x})$, which reflects the fact that there are internal degrees of freedom that transform non-trivially under parity. For a Block state in solids, this corresponds to physical degrees of freedom that transform non-trivially under $\mathcal{P}$, e.g. valley degrees of freedom in momentum space. At the Dirac point $\vec{k} = 0$ the Hamiltonian reads:

$$H_D = \gamma^0 m \tag{5}$$

and the parity operator $\mathcal{P}$ reduces to γ^0 at Dirac point $\vec{k} = 0$ since at zero momentum ψ_k has no $\vec{x}$ dependence anymore. The eigenvalues of $\gamma^0 = \mathcal{P}$ is ± 1. Hence the conduction and valence band states have opposite parity at the Dirac point. Also, as argued previously that the conduction and valence bands themselves are 2-fold degenerate due to Kramers theorem; therefore for massless Dirac fermions these two 2-fold bands are expected to cross each other at $\vec{k} = 0$, giving 4-fold degenerate Dirac node (asymptotically). A regorous discussion of the origin of 4-fold degeneracy in presence of $\mathcal{PT}$-symmetry is presented in [2].

B.   Weyl Equation

One representation is of interest in our context, i.e. the Weyl representation of γ matrices:

$$\gamma^0 = \begin{pmatrix} 0 & \mathbb{1}_{2\times 2} \\ \mathbb{1}_{2\times 2} & 0 \end{pmatrix}, \quad \gamma^i = \begin{pmatrix} 0 & \sigma^i \\ -\sigma^i & 0 \end{pmatrix} \tag{6}$$

3

where σ^i are 2×2 pauli matrices. The Dirac equation under Weyl representation becomes:

$$\begin{pmatrix} -m & i(\partial_0 + \vec{\sigma} \cdot \nabla) \\ i(\partial_0 - \vec{\sigma} \cdot \nabla) & -m \end{pmatrix} \psi = 0 \tag{7}$$

We are interested in the consequences of zero-mass spinors, thus, for massless particle with $m = 0$, this can be viewed as a pair of two-component Weyl spinors with opposite chirality, termed ψ_L and ψ_R, described by Weyl equations [3]:

$$i(\partial_0 - \vec{\sigma} \cdot \nabla)\psi_L = 0, \quad i(\partial_0 + \vec{\sigma} \cdot \nabla)\psi_R = 0 \tag{8}$$

whose stationary Hamiltonian can be compactly written as $H(\vec{k}) = \pm \vec{\sigma} \cdot \vec{p}$. The two equations has opposite chirality. This means that the Weyl fermions, described by two 2-spinors, are massless Dirac fermions with different chirality. In other words, we can understand the Dirac fermions as two degenerate Weyl fermions with opposite chirality.

To articulate the nature of chirality, here we show how to decompose Dirac spinor into chiral Weyl spinors. The chirality operator γ^5 is defined by:

$$\gamma^5 = i\gamma^0\gamma^1\gamma^2\gamma^3 = \begin{pmatrix} -\mathbb{1}_{2\times2} & 0 \\ 0 & \mathbb{1}_{2\times2} \end{pmatrix} \tag{9}$$

γ^5 has several nice and useful properties, i.e. it can be shown that γ^5 is Hermitian, anti-commutes with γ^μ matrices and squares to identity:

$$\left(\gamma^5\right)^\dagger = \gamma^5, \quad \{\gamma^5, \gamma^\mu\} = 0, \quad \left(\gamma^5\right)^2 = \mathbb{1} \tag{10}$$

Next, noting that γ^5 anticommutes with Dirac equation and that it is Hermitian, Dirac spinors can be labelled (decomposed) into right- and left-chiral spinors. Identity can be rewritten as:

$$\mathbb{1} = \frac{1}{2}(\mathbb{1} - \gamma^5) + \frac{1}{2}(\mathbb{1} + \gamma^5) \equiv P_L + P_R \tag{11}$$

where we have defined the left- and right-chiral projection operators $P_{L,R}$, explicitly:

$$P_L = \frac{1}{2}(\mathbb{1} - \gamma^5) = \begin{pmatrix} \mathbb{1} & 0 \\ 0 & 0 \end{pmatrix}, \quad P_R = \frac{1}{2}(\mathbb{1} + \gamma^5) = \begin{pmatrix} 0 & 0 \\ 0 & \mathbb{1} \end{pmatrix} \tag{12}$$

which satisfies $P_R P_L = 0$. It also allows us to decompose a Dirac spinor as:

$$\psi = \mathbb{1}\psi = \frac{1}{2}(\mathbb{1} - \gamma^5) + \frac{1}{2}(\mathbb{1} + \gamma^5) \equiv \psi_L + \psi_R \tag{13}$$

4

where $\psi_{L,R}$ are termed Weyl spinors with opposite chirality. Using $(\gamma^5)^2 = \mathbb{1}$, we immidiately get:

$$P_L\psi = \psi_L, \qquad P_R\psi = \psi_R$$
$$\gamma^5\psi_L = -\psi_L, \quad \gamma^5\psi_R = +\psi_R \tag{14}$$

Thus we see $P_{L,R}$ truely projects the 4-component Dirac spinor ψ into two 2-component Weyl spinors with opposite chiralities.

By setting $c = v_F$, the 3D Weyl Hamiltonian reads:

$$H(\vec{k}) = \pm v_F \vec{\sigma} \cdot \vec{p} = \pm v_F (p_x\sigma_x + p_y\sigma_y + p_z\sigma_z) \tag{15}$$

which respects both $\mathcal{P}$ and $\mathcal{T}$ symmetry. Unlike the 2D Dirac Hamiltonian of graphene whose Dirac point vanishes upon introducing a massive $m\sigma_z$, however, such a band crossing in 3D Weyl Hamiltonian is *robust*. This can be seen from the fact that we can always tune the 3 components of $\vec{k}$ in momentum space such that the gap vanishes, and a massive term $m\sigma_z$ merely moves the location of the band crossing in momentum space. Hence the Weyl Hamiltonain describes massless Weyl fermions with $\pm$ chiralities, and the 3D band crossing is termed Weyl point or Weyl node. If the fermi energy cuts across the Weyl point the system is called Weyl semimetal, whose gapless excitation is called Weyl fermions. This is consistent with the 4-fold degeneracy in Dirac equation, however, the degenerate nodes in Weyl equation are described by 2 chiral plus 2 Kramers degeneracy, in contrast to the 2 parity plus 2 Kramers degeneracy, i.e. the number of degeneracy remains the same as expected, but the contents of such degeneracy is changed by a different representation of γ in Weyl equation. The connection between symmetry and chirality of Weyl nodes plays an important role in the study of Weyl semimetals. As will be discussed in next section, in a $\mathcal{T}$-breaking Weyl semimetal whose Hamiltonian is invariant under $\mathcal{P}$, a Weyl node at $\vec{k}$ is related to the other node at $-\vec{k}$ about the inversion center, and they have opposite chirality; while in a $\mathcal{P}$-breaking Weyl semimetal that preserves $\mathcal{T}$, the time-reversal transformation relates two Weyl nodes with the same chirality.

C. Broken Symmetry

The existence of Weyl semimetal requires the breaking of either time-reveral symmetry $\mathcal{T}$ or inversion symmetry $\mathcal{P}$, or both, such that the band touchings of different chiralities can be
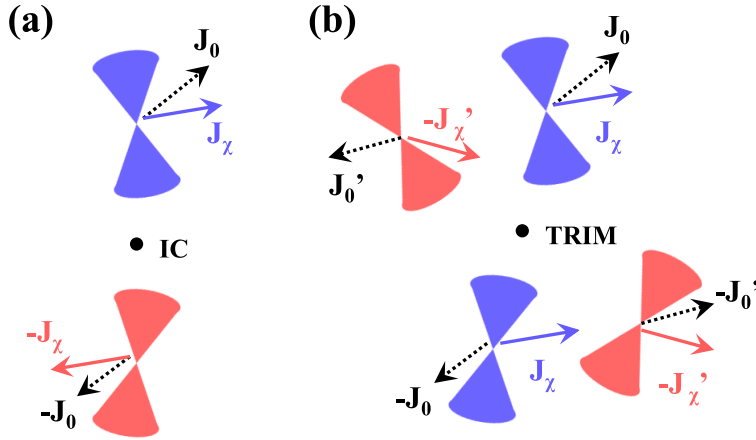
FIG. 1. (a) In $\mathcal{T}$-breaking Weyl semimetals with $\mathcal{P}$-symmetry intact, a pair of $\mathcal{P}$-related Weyl nodes have opposite opposite chirality. (b) In $\mathcal{P}$-breaking Weyl semimetals, $\mathcal{T}$-symmetry relates two Weyl nodes of the same chirality. [4]

seperated in the first Brillouin zone. An important aspect on determining band touching is to analyse the degeneracy of bands by symmetries. (i) If both $\mathcal{P}$ and $\mathcal{T}$ are respected, then the momentum is invariant under the joint transformaion $\mathcal{PT}$, and $(\mathcal{PT})^2 = -1$ ensures the double degeneracy of bands. (ii) If $\mathcal{T}$ is present but $\mathcal{P}$ is broken, then bands are generally non-degenerate since momentum changes sign under $\mathcal{P}$, and only at TRIM is a Kramers degeneracy present. (iii) If $\mathcal{T}$ is broken but $\mathcal{P}$ is present, the bands are generally nondegenerate. Hence, in order for a pair of non-degenerate bands to touch we need to break $\mathcal{P}$ or $\mathcal{T}$ symmetry, or both.

If $\mathcal{P}$ is present we need to break $\mathcal{T}$ symmetry. This allows the band structure with minimum 2 nodes, instead of 4, with opposite chiralities. Since $\mathcal{P}^2 = 1$ the inversion symmetry generally does not introduce the Kramers equal-energy pair like $\mathcal{T}^2 = -1$ does, thus there can be a unique node for each chirality. This gives two nodes with opposite chirality. The schematic band structure is shown in Fig.1(a).

If $\mathcal{T}$ is present then we need to break $\mathcal{P}$ to get a Weyl semimetal. In this case there must be at least 4 Weyl nodes. This is because $\mathcal{T}$ brings a node at $\vec{k}_0$ to another node $-\vec{k}_0$ with $\epsilon_1(\vec{k}_0) = \epsilon_2(-\vec{k}_0) = \mu$ within the same chirality. Since the net chirality has to vanish (Chern number of a $\mathcal{T}$-symmetric system has to vanish), there has to be another pair of Weyl nodes with opposite chirality, giving 4 nodes in total. The schematic band structure is shown in

6

Fig.1(b).

D. Topology

In this section I will present the topological properties of Weyl systems. As a simplest example, I will discuss the geometric phases of Weyl equations and their consequences (Berry phase, connection, curvature and Chern number), and the topologically protected gapless surface states, i.e. the Fermi arcs as an important experimental probe Weyl physics.

1. Berry phase

The topology of the Weyl fermions can be understood by Berry curvature. The simplest Hamiltonian that describes pairs of Weyl nodes with opposite chirality is given by:

$$H(k) = \pm v_F \vec{\sigma} \cdot \vec{k} \tag{16}$$

whose eigen states are (in polar coordinate):

$$|u_R(k, \theta, \phi)\rangle = \begin{pmatrix} \sin\left(\frac{\theta}{2}\right) \\ -e^{-i\phi}\cos\left(\frac{\theta}{2}\right) \end{pmatrix}, \quad |u_L(k, \theta, \phi)\rangle = \begin{pmatrix} \cos\left(\frac{\theta}{2}\right) \\ e^{i\phi}\sin\left(\frac{\theta}{2}\right) \end{pmatrix} \tag{17}$$

for $+1$ and -1 chirality respectively. Here I briefly sketch the calculation of $|_R\rangle$ with chirality $= +1$. To obtain Berry connection, we have

$$\nabla_k |u_R(k, \theta, \phi)\rangle = \frac{\hat{e}_\theta}{k}\begin{pmatrix} \frac{1}{2}\cos\left(\frac{\theta}{2}\right) \\ \frac{1}{2}e^{i\phi}\sin\left(\frac{\theta}{2}\right) \end{pmatrix} + \frac{\hat{e}_\phi}{2k}\begin{pmatrix} 0 \\ -ie^{i\phi}/\sin\left(\frac{\theta}{2}\right) \end{pmatrix} \tag{18}$$

thus the Berry connection and Berry curvature are:

$$\mathcal{A} = i\langle u_R|\nabla_k u_R\rangle = -\frac{\cos^2\left(\frac{\theta}{2}\right)}{k\sin\theta}\hat{e}_\phi, \quad \mathcal{B} = \nabla_k \times \mathcal{A} = \frac{\hat{e}_k}{2k^2} \tag{19}$$

Choosing a spherical shell in momentum space that encloses the Weyl node (at $\vec{k} = 0$ in the simplest case), we find the Berry phase, i.e. the total flux is

$$\gamma = \int_0^{2\pi} d\phi \int_0^\pi \mathcal{B}\, k^2 \sin\theta d\theta = 2\pi \tag{20}$$

Thus the Chern number is $\mathcal{C}^+ = +1$. Similarly, the Chern number for $|u_L\rangle$ with chirality $= -1$ is $\mathcal{C}^- = -1$, and its Berry curvature has an negative sign compared to $|u_R\rangle$. Since the
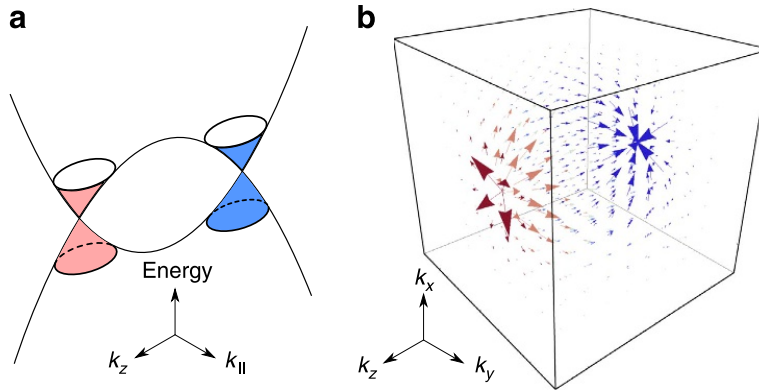
7

FIG. 2. Band structure and Berry curvature of a pair of Weyl nodes with opposite chirality. (a) A schematic diagram of band structures of 2 seperated Weyl nodes. (b) The vector plot of the Berry curvature. The arrows show that the flux of the Berry curvature flows from one monopole (red) to the other (blue) [5]

flux through the Fermi surface enclosing the Weyl node is non-zero, by Gauss' law the Weyl node may be interpreted as a monopole charge [6]. For the case of the right-handed chiral spinor with chirality $+1$ has $\mathcal{C} = +1$, and left-handed chiral spinor has $\mathcal{C} = -1$. Hence, the Chern number can be regarded as a topological charge of the Weyl node where the sign of the charge is determined by the chirality, and Berry curvature, i.e. the k-space magnetic field, flows from one monopole to the other, as shown in Fig.2.

2. Fermi Arcs

In integer quantum Hall states or topological insulators, there is a bulk-edge correspondence saying there is a finite energy gap in the bulk while gapless excitations on surface (edge). On the contrary, the Weyl semimetal has a stable band crossing that can not be gapped out by breaking symmetries, which brings about the questions: does Weyl semimetal have topologically protected gapless surface states? In this section, we are going to show that there *are* indeed topologically protected gapless surface states in Weyl semimetals known as Fermi arcs.

Surface states are common in band insulators, in which surface states can exist within the bulk band gap and are typically exponentially localized near the surface or interface. While
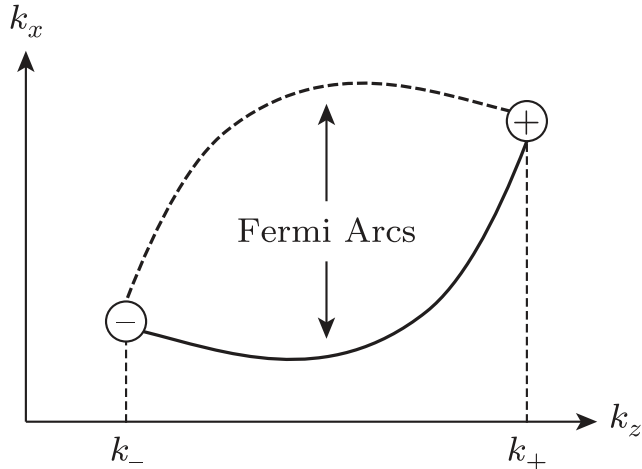
FIG. 3. Illustration of Fermi arcs at the surfaces of a Weyl semimetal with only two Weyl points. They connect the projections of the two Weyl points onto the $k_x k_y$ plane, denoted by circles. As one approaches these circles, the gap for the bulk states gets smaller and smaller, and hence the surface states penetrate deeper and deeper into the bulk. At the circles the surface states are completely mixed up with bulk states (or "disappear" into the bulk), allowing the arcs of opposite surfaces to be connected via the bulk. [8]

in Weyl semimetal, we can still define gapless surface states despite that its bulk also being gapless. The Fermi surface of a WSM on a slab consists of unusual states known as Fermi arcs that are essentially a 2D Fermi surface; however, part of this Fermi surface is glued to the top surface and the other, to the bottom [7]. In 3D Weyl semimetal the surface states live within the 2D surface Brillouin zone (sBZ). Assume there is a pair of Weyl nodes with opposite chiralities at $k_z = k_{\pm}$ respectively. Then k_z can be viewed as a tunable parameter which produces slices of 2D *gapped* bands within the sBZ if $k_z \neq k_{\pm}$, which is similar to the 2D Dirac Hamiltonian gapped by $m\sigma_z$ with m substituted by k_z. Therefore one can define a k_z-dependent Chern number $\mathcal{C}(k_z)$ as a topological quantum number, which can only change when k_z sweeps across band-crossings at $k_z = k_{\pm}$. The two band crossings in sBZ are indicative of a different $\mathcal{C}$ in the range of $k_- < k_z < k_+$ and that in the complement momentum range. In fact, a Weyl Hamiltonian produces $\mathcal{C} = 1$ for $k_- < k_z < k_+$ and $\mathcal{C} = 0$ otherwise. A band that carries $\mathcal{C} \neq 0$ must have $|C|$ branches of chiral edge modes, indicating gapless edge states for $k_- < k_z < k_+$. Fermi arcs are a valuable theoretic tool in

9

the search of Weyl semimetals. A schematic illustration of a pair of Weyl points and Fermi arcs are shown in Fig.3. This picture helped to identify TaAs as a Weyl semimetal using ARPES, whose experimental data and other details are shown in [9, 10].

III. NONLINEAR OPTICAL PROBE

In this section, I will discuss the nonlinear optical effects that are able to give insights to Weyl semimetals. These effects are non-linear in the sense that the response of the material to the applied field depends nonlinearly on the field. In general, nonlinear effects such as second harmonic generation (SHG) are intimately related to the Berry connection and Berry curvature. Morimoto [11] predicted that optical transitions that occur near Weyl nodes between bands with nearly linear dispersion should give a near universal prediction in the low frequency limit for the nonlinear susceptibility. In the following, I present the basic notion of SHG and the way it is related to Berry connection of Floquet bands.

A. Introduction to Non-linear Response

Consider a set of generic optical susceptibility tensors $\chi_{ijk}^{(i)}$, the response is described by the relation

$$P_i(t) = \chi_{ij}^{(1)} E_j + \chi_{ijk}^{(2)} E_j E_k + \chi_{ijkl}^{(3)} E_j E_k E_l + \mathcal{O}(E^4) \tag{21}$$

where P is a generic response in i-th direction of a material, e.g. current density or the dipole moment density. The SHG is thus characterized by

$$P_i^{(2)}(2\omega) = \chi_{ijk}^{(2)} E_j(\omega) E_k(\omega) \tag{22}$$

SHG can be thought of in terms of the interaction between material and fields, in which photons are exchanged between various frequency components of the field. For example, the input of a monochromatic light with fixed frequency ω into a material gives the output current with a frequency of 2ω. For a generic non-linear process, the output spectrum may contain modes with other frequencies. A schematic illustration of SHG is shown in Fig.4. In this article, we assume the dispersion of the second order susceptibitlity can be neglected. By defining the tensor $d_{ijk} \equiv (1/2)\chi_{ijk}^{(2)}$ the SH response can be written as

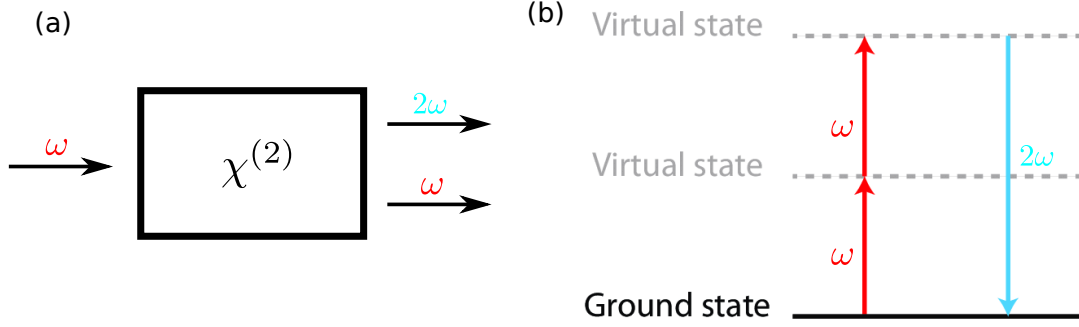$$P_i(2\omega) = 2d_{ijk} E_j(\omega) E_k(\omega) \tag{23}$$

FIG. 4. (a) Geometry of second-harmonic generation. (b) Energy-level diagram describing second-harmonic generation.

where the upper index of $P_i^{(2)}$ is suppressed for simplicity, and Einstein rule is assumed. It is clear that the tensor d_{ijk} must be symmetric in its last two indices, since there is no physical way to distinguish 2 copies of the same field. Therefore we can define a contracted notation d_{il} according to [12]

$$
\begin{array}{cccccc}
jk: & 11 & 22 & 33 & 23,32 & 31,13 & 12,21 \\
l: & 1 & 2 & 3 & 4 & 5 & 6
\end{array}
\tag{24}
$$

We can then express the SH response using the matrix equation

$$
\begin{pmatrix} P_1(2\omega) \\ P_2(2\omega) \\ P_3(2\omega) \end{pmatrix} = 2 \begin{pmatrix} d_{11} & d_{12} & d_{13} & d_{14} & d_{15} & d_{16} \\ d_{21} & d_{22} & d_{23} & d_{24} & d_{25} & d_{26} \\ d_{31} & d_{32} & d_{33} & d_{34} & d_{35} & d_{36} \end{pmatrix} \begin{pmatrix} E_1(\omega)^2 \\ E_2(\omega)^2 \\ E_3(\omega)^2 \\ 2E_2(\omega)E_3(\omega) \\ 2E_1(\omega)E_3(\omega) \\ 2E_1(\omega)E_2(\omega) \end{pmatrix}
\tag{25}
$$

where the factor of 2 in the last column comes from the equivalent permutations of last two indices of d_{ijk}. For a fixed propagation and polarization directions, as is often the case in optical experiments, we can define a convenient effective tensor d_{eff}, so that the SHG can be characterized by

$$
P(2\omega) = 2d_{eff}E(\omega)^2, \quad \text{with } E(\omega)^2 = ||\mathbf{E}(\omega)||^2 = \sum_i E_i(\omega)^2
\tag{26}
$$

The calculation of d_{eff} from d_{il} varies in different crystall classes. The general recipe of d_{eff} for different point groups has been developed by Midwinter and Warner.

Another property of SHG that is crucial for the goal of this article is the influence of inversion or parity symmetry, which is often broken in Weyl semimetals. That is: a non-trivial SHG requires the broken of $\mathcal{P}$-symmetry. It can be readily proved from Eq.(23) in the following way. The polarizable response P_i changes sign under $\mathcal{P}$, that is $\mathcal{P}P_i = -P_i$. The field also transforms in the same way $\mathcal{P}E_j = -E_j$, and the susceptibitlity is invariant under inversion. These together gives

$$- P_i(2\omega) = 2d_{ijk}[-E_j(\omega)][-E_k(\omega)] = 2d_{ijk}E_j(\omega)E_k(\omega) \tag{27}$$

comparing with Eq.(23) we have

$$d_{ijk} = 0, \quad \chi^{(2)}_{ijk} = 0 \tag{28}$$

if $\mathcal{P}$ is respected. Therefore the inversion symmetry must be broken in order for SHG to occur. This property plays a crucial role in the study of non-linear optical effects in inversion-breaking materials, e.g. the Weyl semimetal.

B. Floquet Two-Band Model

Driven by the time dependent gauge field, the non-equalibrium state exhibit a gapped anticrossing bewteen a valence band dressed with photon and conduction band without photon, which is shown in Fig.5. To see this, we first derive the Floquet Hamitonian $\mathcal{H}$. For simplicity, let us consider a system coupled to a linearly polarized gauge field $A(t) = iAe^{-i\Omega t} - iA^*e^{i\Omega t}$, with $A = E/\Omega$. The time-dependent Hamiltonain is given by

$$H(t) = H_0(k + A(t)) \tag{29}$$

where H_0 is the original Hamiltonian without the time-dependent drive. Then we keep terms up to the linear order of A

$$H(t) \simeq H_0(k) + A(t)v^0 \tag{30}$$

where we have defined v^0 as

$$v^0 = \partial H_0/\partial k \tag{31}$$

Next we recast this linearied Hamiltonian into a Fourier-space Floquet Hamiltonain H_{mn}. The Floquet Hamiltonian reads

$$\mathcal{H} = H(t) - i\frac{\partial}{\partial t} \quad \xrightarrow{F.T.} \quad \mathcal{H}_{mn} = H_{mn} - n\Omega\delta_{mn} \tag{32}$$
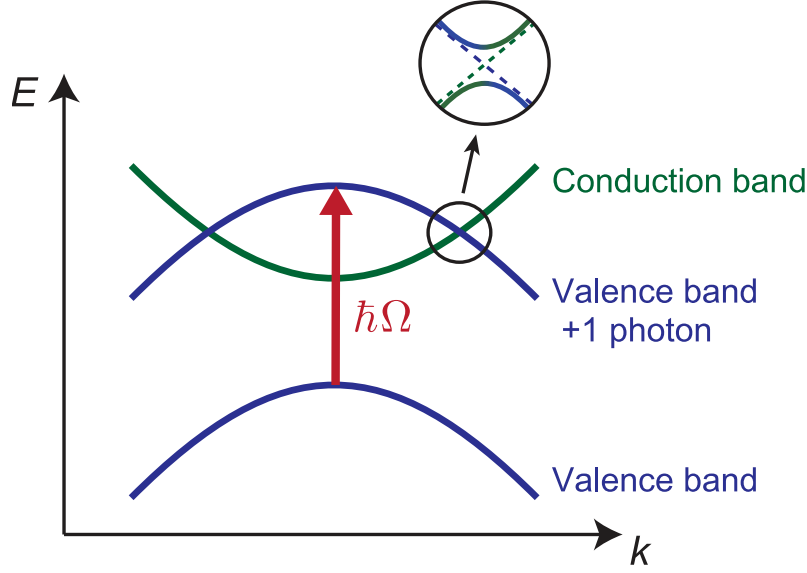
12

FIG. 5. Schematic picture of the Floquet two band model. Under the drive of monochromatic light, energy bands evolve into Floquet bands, which describe Bloch states dressed with photons. When two Floquet bands cross, they show an anticrossing. The nonequilibrium steady state can be captured by studying this anticrossing of two Floquet bands. [11]

where we have set $\hbar = 1, e = 1$ for simplicity. We can expand $\mathcal{H}$ in momentum space with the Floquet modes $|\Phi_\alpha(t)\rangle = \sum_m \exp\{-im\Omega t\} |u_\alpha^m\rangle$, which gives

$$H_{mn} = \frac{1}{T} \int_0^T dt \ \exp\{i(m-n)\Omega t\} H(t) \tag{33}$$

thus the Floquet Hamiltonian is

$$\mathcal{H}_{mn} = \frac{1}{T} \int_0^T dt \ \exp\{i(m-n)\Omega t\} H(t) - n\Omega \delta_{mn} \tag{34}$$

H_{mn} and $\mathcal{H}_{mn}$ are time independent but has an additional matrix structure spanned by Floquet modes, that is, for each index pair (m, n) we have a matrix operator $\hat{H}_{mn}$, which satisfies the Floquet equation in Fourier space, and that the quasienergy of the α-band dressed with a Floquet m-mode is $\tilde{\epsilon}_\alpha = \epsilon_\alpha + m\Omega$:

$$\sum_n H_{mn} |u_\alpha^n\rangle = (\epsilon_\alpha + m\Omega) |u_\alpha^m\rangle \tag{35}$$

and equivalently

$$\sum_n \mathcal{H}_{mn} |u_\alpha^n\rangle = \epsilon_\alpha |u_\alpha^m\rangle \tag{36}$$

13

Hence it is convenient to label steady states by a pair of integers (α, m), denoting the α-band dressed with m photons. Next let us determine the matrix elements of Floquet Hamiltonian (under monochramatic drive), that is, expanded in the basis of the harmonic components. The matrix is sparse noting that (i) $H(t)$ is driven by monochramatic gauge field so that elements with $|m - n| > 1$ will vanish, and (2) for $m = n$ we have $1/T \int H(t) = H_0$, i.e. the time-independent unperturbed Hamiltonain. Hence the Floquet Hamiltonian has the structure:

$$
\begin{pmatrix}
& \vdots & \vdots & \vdots & \vdots & \vdots & & \vdots & \vdots & \\
\dots & P^\dagger & H_0 + 2\Omega & P & 0 & 0 & & 0 & 0 & \dots \\
\dots & 0 & P^\dagger & H_0 + \Omega & P & 0 & & 0 & 0 & \dots \\
\dots & 0 & 0 & P^\dagger & H_0 & P & & 0 & 0 & \dots \\
\dots & 0 & 0 & 0 & P^\dagger & H_0 - \Omega & & P & 0 & \dots \\
\dots & 0 & 0 & 0 & 0 & P^\dagger & & H_0 - 2\Omega & P & \dots \\
& \vdots & \vdots & \vdots & \vdots & \vdots & & \vdots & \vdots &
\end{pmatrix}
\begin{pmatrix} \vdots \\ u_\alpha^{-2} \\ u_\alpha^{-1} \\ u_\alpha^{0} \\ u_\alpha^{1} \\ u_\alpha^{2} \\ \vdots \end{pmatrix}
= \epsilon_\alpha
\begin{pmatrix} \vdots \\ u_\alpha^{-2} \\ u_\alpha^{-1} \\ u_\alpha^{0} \\ u_\alpha^{1} \\ u_\alpha^{2} \\ \vdots \end{pmatrix}
\tag{37}
$$

where we have defined

$$
P = \frac{1}{T} \int_0^T dt \, e^{\pm i\Omega t} H(t)
\tag{38}
$$

We further ignore all but two Floquet modes, that is, the Floquet index $m = -1$ and the other one with $m = 0$, i.e. dressing of one photon and zero photon. Hence the low-modes effective matrix in Eq.(37) is truncated such that only two bands are evolved. For simplicity, we label the valence band with integer 1, and conduction band with integer 2. For simplicity we label the valence band by $|u_1^{-1}\rangle \equiv |u_1\rangle$, and the conduction band by $|u_2^0\rangle \equiv |u_2\rangle$. If $A \neq 0$, these two Floquet bands are locally connected by an anti-crossing, which is captured by the following effective Hamiltonian:

$$
\mathcal{H}_F = \begin{pmatrix} \epsilon_1^0 + \Omega & -iA^* v_{12}^0 \\ iA v_{21}^0 & \epsilon_2^0 \end{pmatrix} \equiv \epsilon + \vec{d} \cdot \vec{\sigma}
\tag{39}
$$

and the effective identity in this 2-level system reads

$$
|u_1\rangle \langle u_1| + |u_2\rangle \langle u_2| = \mathbb{1}
\tag{40}
$$

This is the basic setup of our question: What is the spectrum of the response current J as a function of frequency in such photon-assisted process described by the Floquet two-band model. In the next subsections, I'm going to discuss the DC current J and second harmonic generation $J(2\omega)$ based on what has been introduced.

1. Nonlinear DC response

Let us discuss the simplest case first, i.e. DC current, and the higher harmonic generation follows in a similar logic thereafter. The DC current operator is then given by

$$\tilde{v} = \frac{\partial \mathcal{H}_F}{\partial k} = \begin{pmatrix} v_{11}^0 & -iA^* \left(\frac{\partial v^0}{\partial k} \right)_{12} \\ iA \left(\frac{\partial v^0}{\partial k} \right)_{21} & v_{22}^0 \end{pmatrix} \equiv b_0 + \vec{b} \cdot \vec{\sigma} \tag{41}$$

by Hellmann-Feynman theorem the matrix element of v^0 can be written as

$$\begin{aligned} \left(\frac{\partial v^0}{\partial k} \right)_{12} &= \frac{\partial v_{12}^0}{\partial k} - \left\langle \frac{\partial u_1}{\partial k} \middle| v^0 \middle| u_2 \right\rangle - \left\langle u_1 \middle| v^0 \middle| \frac{\partial u_2}{\partial k} \right\rangle \\ &= v_{12}^0 \left(\frac{\partial}{\partial k} \log v_{12}^0 + i\mathcal{A}_1 - i\mathcal{A}_2 + \frac{v_{11}^0 - v_{22}^0}{\epsilon_1 - \epsilon_2} \right) \end{aligned} \tag{42}$$

where $\mathcal{A}_i$ is the Berry connection of i-th band given by $\mathcal{A}_i = -i \langle u_i | \partial_k u_i \rangle$. Now we are ready to show the current expectation given by

$$J = -i \operatorname{Tr}(\tilde{v} G^<) \tag{43}$$

as is explained in Supplemental. D 2, where $G^<$ is the lesser Green's function in the Keldysh formalism [13, 14], which is given for the two-band model as [11]

$$G^< = \frac{(\omega - \epsilon + i\Gamma/2 + \vec{d} \cdot \vec{\sigma}) \Sigma^< (\omega - \epsilon - i\Gamma/2 + \vec{d} \cdot \vec{\sigma})}{[(\omega - \epsilon + i\Gamma/2)^2 - d^2][(\omega - \epsilon - i\Gamma/2)^2 - d^2]} \tag{44}$$

where $\Sigma^<$ is the lesser self-energy given by $\Sigma^< = i\Gamma(1 + \sigma_z)/2$. If the time-reversal symmetry $\mathcal{T}$ is respected, the current expectation is obtained as

$$J = \int d\vec{k} \frac{\Gamma}{2} \frac{d_y b_x - d_x b_y}{d^2 + \Gamma^2/4} \tag{45}$$

where the numerator is

$$\begin{aligned} d_y b_x - d_x b_y &= \operatorname{Im}[(d_x + id_y)(b_x - ib_y)] = |A|^2 \operatorname{Im} \left[v_{21}^0 \left(\frac{\partial v^0}{\partial k} \right)_{12} \right] \\ &= |A|^2 |v_{12}^0|^2 R_k \end{aligned} \tag{46}$$

where in the last row we used Eq.(42) and defined the shift current R_k as

$$R_k \equiv \frac{\partial \phi_{12}}{\partial k} + \mathcal{A}_1 - \mathcal{A}_2, \quad \phi_{12} \equiv \operatorname{Im}[\log v_{12}^0] \tag{47}$$

After some algebra we arrive at the photocurrent in the second order of driving field under time-reversal symmetry

$$J = \frac{\pi |E|^2}{\Omega^2} \int d\vec{k} \, \delta(\epsilon_1^0 - \epsilon_2^0 + \omega) |v_{12}^0|^2 R_k \tag{48}$$

15

so the conductivity of DC current is determined by Berry connections in R_k. In fact, as will be discussed in the next subsection, the second harmonic current response can be determined in the same way and is related to the shift vector R_k in a similar manner.

2. Second-harmonic response

The second-harmonic generation (SHG) is the nonlinear current response with the frequency 2Ω induced by a monochromatic light. In order to capture the 2nd order contribution of the driving field we need to expand $H(t)$ to the second order of $A(t)$:

$$H(t) = H_0(k) + A(t)v^0 + \frac{1}{2}A^2(t)\partial_k v^0 + \mathcal{O}(A^3) \tag{49}$$

we are interested in the 2nd harmonic contribution, that is, valence and conduction band are labelled by $m = -2$ and $m = 0$, with $P = 1/T \int dt \exp\{\pm i2\Omega t\}H(t)$. Follow the same reasoning in the previous subsection, the Floquet two-band model for SHG is

$$\mathcal{H}'_F = \begin{pmatrix} \epsilon_1^0 + 2\Omega & -\frac{1}{2}(A^*)^2 \left(\frac{\partial v_{12}^0}{\partial k} \right) \\ -\frac{1}{2}A^2 \left(\frac{\partial v_{21}^0}{\partial k} \right) & \epsilon_2^0 \end{pmatrix} \equiv d'_0 + \vec{d}' \cdot \vec{\sigma} \tag{50}$$

The generic current response is described by

$$J(t) = \sum_m -i \operatorname{Tr}[v(t)G^<_{mn}]e^{-i(m-n)\Omega t} \tag{51}$$

with $v(t) = \partial H_0/\partial k$, and it includes different harmonic generations determined by the exponent. Then it is derived that the contribution from 2Ω is

$$J(2\Omega) \simeq \frac{\pi E^2}{2\Omega^2} \int d\vec{k} \left| v_{12}^0 \right|^2 R_k \left[-\delta(\epsilon_1^0 - \epsilon_2^0 + \Omega) + \frac{1}{2}\delta(\epsilon_1^0 - \epsilon_2^0 + 2\Omega) \right] \tag{52}$$

note that the R_k in the integrand, as is defined in Eq.(47), is gauge-invariant, where the dressing of the difference in Berry connection between two bands to the k-derivative makes it equivalent to a covariant derivative that's not affected by non-trivial parallel translation for the Bloch wavefunctions in k. Eq.(52) indicates that the interband contribution to the SHG is characterized by the shift vector R_k, which is related by the Berry connections of Bloch electrons.

16

IV. OPTICAL RESPONSE IN WEYL MATERIALS

Based on the reasoning in Sec.II it may appear that all we need to do to realize a Weyl semimetal is to find a 3D crystal with some symmetries broken. While indeed the band structure of Weyl nodes are quite natural, the material also need to satisfy the requirement that the filling be close to the Fermi energy [15]. One of such material is tantalum arsenide (TaAs) [9, 10], in which Fermi arcs on the surface are observed directly by photoemission spectroscopy. See Fig.S1 in Appendix. In this section, I will dicuss the recent experimental discovery of the giant anisotropic SHG in TaAs, and present it's quantitative explanation using the theory introduced in Section.III.

A. Experiments

Transition metal monopnictides (TMMPs) such as TaAs, a class of noncentrosymmetric materials has been reported to exhibit Weyl physics. Using photoemission spectroscopy one can directly sees Fermi arcs of surface states which terminate on the Weyl nodes [9, 10].

TMMPs are inversion-breaking crystals, hence it can exhibit non-linear optical polarizability and second harmonic generation (SHG). In 2016 Wu *et al* [1] reported a giant, anisotropic optical response $\chi^{(2)}$ in TMMPs TaAs, TaP, NbAs by measurements of SHG, which is larger than in any exsiting literature. These crystals has $4mm = C_{4v}$ point group structure; therefore there are 4 groups of non-vanishing elements: zzz, $zxx = zyy$, $xxz = yyz$, $xzx = yzy$. Since the last two indices are free to permutatem, there are in fact only 3 independent non-zero tensor elements:

$$d_{33} \equiv \frac{1}{2}\chi_{zzz}, \quad d_{31} \equiv \frac{1}{2}\chi_{zxx} = \frac{1}{2}\chi_{zyy}, \quad d_{15} \equiv \frac{1}{2}\chi_{xzx} = \frac{1}{2}\chi_{yzy} = \frac{1}{2}\chi_{xxz} = \frac{1}{2}\chi_{yyz} \qquad (53)$$

In Wu's experiment, polarizers and waveplates are mounted on rotating stages which allows continuous and independent control of the polarization of the generating and SH light that reached the detector. From the $4mm$ structure the SHG intensity is obtained in the appendix of [3]

$$I = \frac{1}{27}\left|d_{eff}\cos^2\theta_1 + 3d_{31}\sin^2\theta_1\right|^2, \quad \frac{1}{3}|d_{15}|^2\sin^2 2\theta_1 \qquad (54)$$

for analysers parallel to $[1, 1, -1]$ and $[1, -1, 0]$ direction respectively, $d_{eff} = d_{33} + 2d_{31} + 4d_{15}$, and θ_1 is the angle of the polarization plane after the generator. By fitting the intensity data
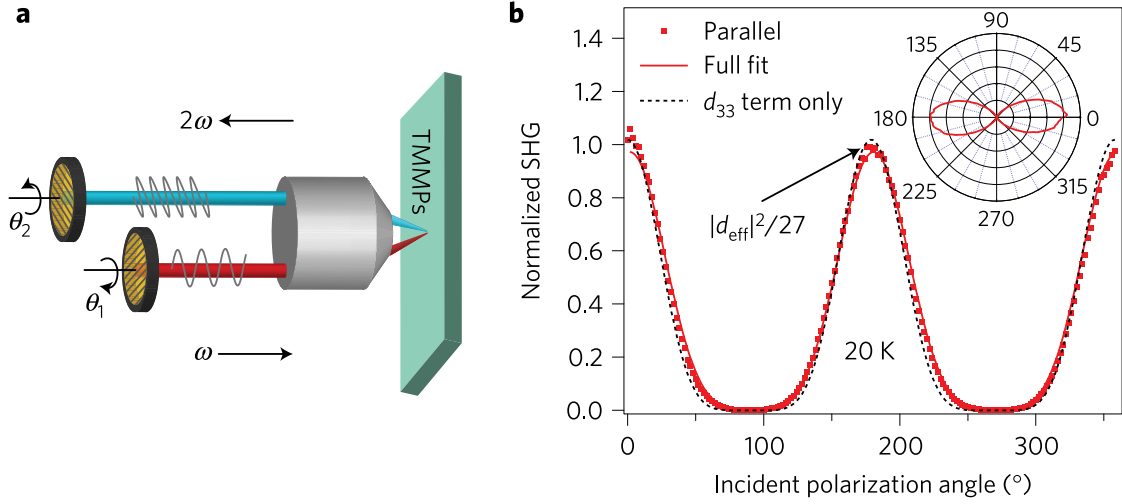
FIG. 6. Second-harmonic generation versus angle as TaAs is effectively rotated about the axis perpendicular to the (112) surface. (a) Schematic of the SHG experimental set-up. θ_1, θ_2 are the angles of the polarization plane after the generator and the analyser. (b) SHG intensity as a function of angle of incident polarization at 20K. The analyser is parallel to the generator. [1]

to these expression one can determine $|d_{eff}/d_{15}|$ and $|d_{eff}/d_{31}|$, and by setting both generator and analyser parallel to the polar axis d_{33}, thus the relative magnitude $|d_{33}/d_{31}|$, $|d_{33}/d_{15}|$, can be obtained. The angular scans indicate that d_{33}, which descibes the response when both generator and analyser are parallel to the polar axis, is much larger than d_{31} and d_{12}, thus contributes most to the SHG intensity. The data of second-harmonic generation v.s. angle is shown is Fig.6. There are two striking phenomena reflected in the data. (i) There is an extreme anisotropy of $\chi^{(2)}$ (ii) an exceptionally giant absolute intensity of SHG response in d_{33} compared to other materials. The comparison of the polarizability and SHG intensity between TaAs and other polar materials is shown is Fig.S2 which visualizes the extreme anisotropy of SHG.

The exceptionally large χ_{zzz} component raises the question of why TMMPs exhibit such an extreme anisotropy. This can be explained semi-quantitatively using the Floquet formalism introduced in Sec.III.

18

B. Model

We consider the following minimal model for a time-reversal symmetric Weyl Hamiltonian with four Weyl nodes

$$H = t \left\{ [\cos k_x a + m_y(1 - \cos k_y a) + m_z(1 - \cos k_z a)]\sigma_x \right.$$
$$\left. + [\sin k_y a + \Delta \cos(k_y a)S_x]\sigma_y + \sin(k_z a)S_x\sigma_z \right\} \quad (55)$$

where σ and S are orbital and spin degrees of freedom respectively. t is a measure of bandwidth, a is the lattice constant, m_y, m_z are parameters that introduce anisotropy, and Δ introduces inversion symmetry breaking. Under $\mathcal{T}$ we have $\vec{k} \to -\vec{k}$, $\vec{\sigma}_y \to -\vec{\sigma}_y$, $\vec{\sigma}_x \to \vec{\sigma}_x$, $\vec{\sigma}_z \to \vec{\sigma}_z$, $\vec{S} \to -\vec{S}$. Under $\mathcal{P}$ we have $\vec{k} \to -\vec{k}$, $\sigma_i \to \sigma_x^{-1}\sigma_i\sigma_x$, $\vec{S} \to \vec{S}$. Then it's readily to check $\mathcal{T}$ is preseved, and only Δ breaks $\mathcal{P}$.

A non-zero Δ seperate a doubly degenerate node into two nodes with opposite chirality, which is shown in Fig.7(a). and, as is mentioned in Sec.III, since $\mathcal{T}$ is preserved, then each chirality shares two Weyl nodes that are related by the $\mathcal{T}$ transformation. If $\Delta = 0$ so that $\mathcal{P}$ is present, pairs of Weyl nodes are located at $\vec{k} = (\pm\pi/2a, 0, 0)$. If $\Delta \neq 0$, then each doubly degenerate node is lifted to two Weyl nodes with opposity chirality seperated by $\Delta k_y \simeq \Delta/a$. The four Weyl nodes of the model can be seen in Fig.7(a,b). We can apply the non-linear theory in Sec.III to this toy Weyl Hamiltonian and evaluate the susceptibility thereafter.

From Eq.(52) the SH conductivity can be understood as an average of $v^2 R$ which is expressed by

$$\sigma_{zzz}^{(2)}(2\omega) \propto \frac{1}{\omega^2} \int d^3\vec{k} \, |v_{z,12}|^2 R_{zz}(\vec{k}) \equiv \langle v^2 R \rangle / \omega^2 \quad (56)$$

Let the indices $1, 2$ denote the valence and conduction band in Floquet formalism. R_{zz} in Eq.(56) is the shift vector defined as $R_{zz} = \partial_{k_z}\phi_{z,12} + \mathcal{A}_{z,1} - \mathcal{A}_{z,2}$ with $\phi_{1,2} = \text{Im}[\log v_{12}]$ and $\mathcal{A}$ the Berry connection. Note that $\sigma_{zzz}^{(2)}$ has odd parity due to the oddness of the shift vector, thus it will vanish as $\Delta \to 0$ at which inversion symmetry is preserved. In the classical picture, SH polarization $P(\omega) = P\exp\{2i\omega t\}$ can be viewed as an electric dipole giving rise to the SH current $J(\omega) = J\exp\{2i\omega t\}$, which are related by

$$P(\omega) = \epsilon_0\chi_{zzz}^{(2)}E_z^2, \quad J(\omega) = \sigma_{zzz}^{(2)}E_z^2, \quad J(\omega) = \partial_t P(\omega) \quad (57)$$

therefore the second order conductivity is related to the SH susceptibility by

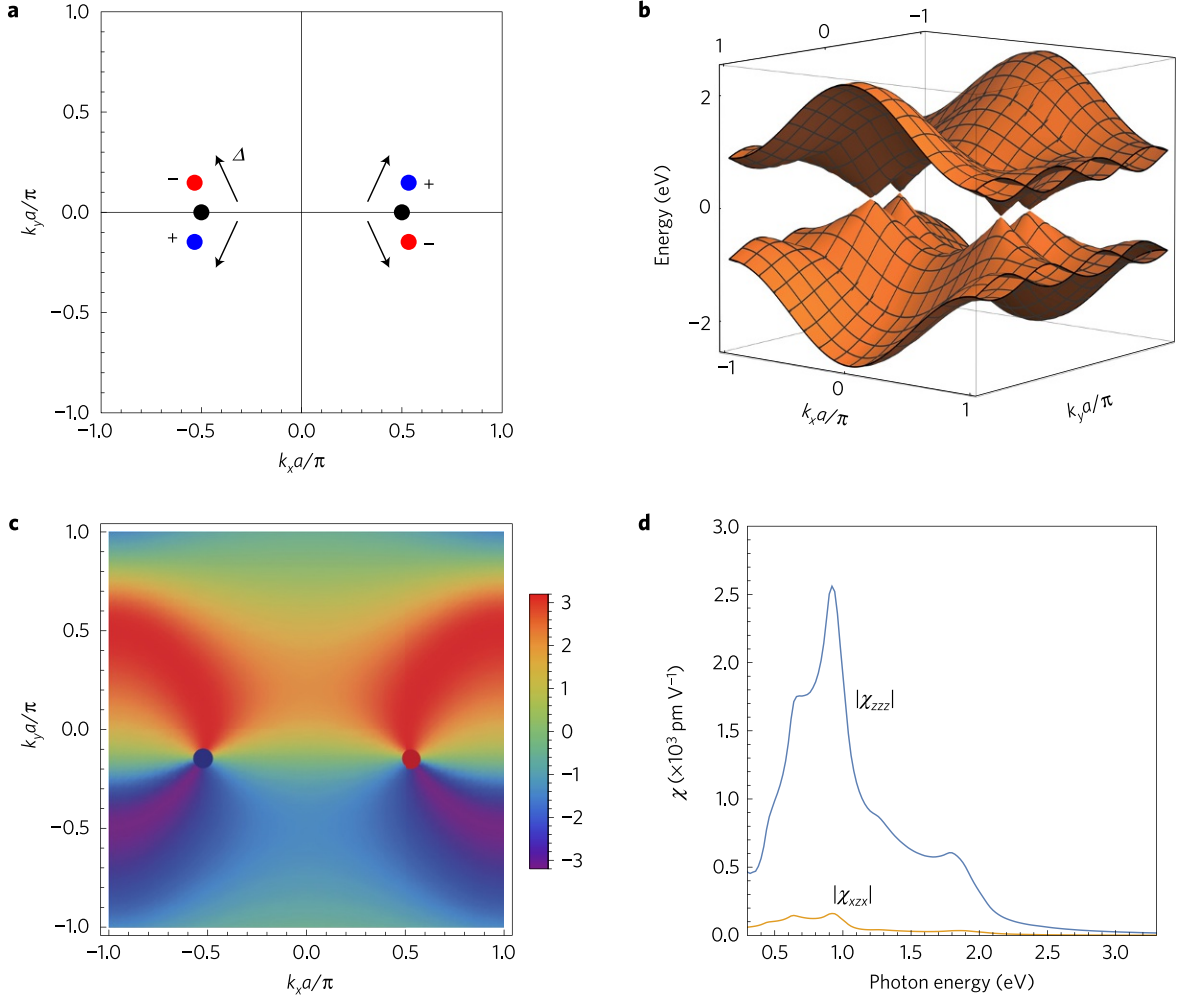$$\chi^{(2)} = \sigma^{(2)}/2i\omega\epsilon_0 \quad (58)$$

19

FIG. 7. Numerical results relevant for the Hamiltonian in Eq.(55) (a) Location of Weyl points in the $k_z = 0$ plane for $\Delta = 0.5$. For $\Delta = 0$, Weyl points with opposite chiralities are located at $(\pm \pi/2a, 0, 0)$. (b) The band structure for $\Delta = 0.5$ and $k_z = 0$, the four band touching corresponds to the four Weyl nodes shown in the previous panel. (c) Color plot of $v_{12}^2 R_z z$, for $S_x = +1$ bands with Weyl points at $k_y < 0$. (d) susceptibility in zzz and xzx polarization, i.e. χ_{zzz} and χ_{xzx} as a function of photon energy, with parameters being $\Delta = 0.5$, $t = 0.8eV$, $m_y = 1$, $m_z = 5$. [1]

Morimoto and Wu predicted that optical transitions near Weyl nodes between 2 nearly-linearly bands gives a universal expression for the non-linear susceptibility in low ω as:

$$\chi^{(2)} = \frac{g(\omega) \langle v^2 R \rangle}{2i\omega^3 \epsilon_0} \tag{59}$$

as a result of Eq.(58) and that in low frequency limit $\sigma^{(2)} \rightarrow g(\omega) \langle v^2 R \rangle /\omega^2$, where $g(\omega)$ is the density of states near Weyl nodes. It is simple to show that the Weyl density of states

20

near a Weyl node with 3D linear dispersion exhibits

$$g(\omega) = \frac{\omega^2}{2\pi^2 v_F^3} \tag{60}$$

with v_F being the Fermi velocity. Hence we have $g(\omega) \propto \omega^2$; therefore, in low energy regime where the momentum averaged $\langle v^2 R \rangle$ will be a non-zero value, the SHG susceptibility should scale as

$$\chi^{(2)} \to \frac{g(\omega) \langle v^2 R \rangle}{\omega^3} \propto \frac{1}{\omega} \tag{61}$$

This $1/\omega$ divergence is a unique signature in inversion-breaking Weyl semimetals due to the 3D linear dispersion near Weyl nodes, and can result in the huge anisotropic susceptibility as $\omega \to 0$. However, in real materials with disorder or impurities, $g(\omega = 0)$ will acquire a non-zero value[16, 17], hence the SHG divergence is expected to be cut off at low frequencies. This accounts for the giant anisotropic $\chi^{(2)}$ at 800nm, instead of $\omega \to 0$, in TMMPs reported by Wu *et al.*

The numerical results relevant for the Hamiltonian in Eq.(55) are shown in Fig.7. The anisotropy of susceptibility is shown in Fig.7(d), where χ_{zzz} is much larger than χ_{xzx} at low frequency regime which. This agrees with the theoretical prediction that SHG susceptibility scales as $1/\omega$ as $\omega \to 0$.

V. CONCLUSION

In this paper, I presented the fundamental aspects of Weyl semimetals and their unique topological characteristics. I discussed the fundamental aspects of non-linear optical effects, especially the second harmonic generation by Floquet band model, which is strong in inversion-breaking Weyl semimetals. Using the SHG by a Floquet two band model, I presented how the giant anisotropic optical response in TaAs may be related to the Berry connections of the two bands involved in the optical transition.

------

[1] Wu, L. *et al.* Giant anisotropic nonlinear optical response in transition metal monopnictide weyl semimetals. *Nature Physics* **13**, 350–355 (2017). URL https://doi.org/10.1038/nphys3969.

[2] Witten, E. Three lectures on topological phases of matter (2015). URL https://arxiv.org/abs/1510.07698v2. 1510.07698.

[3] Weyl, H. Elektron und gravitation. i. *Zeitschrift für Physik* **56**, 330–352 (1929). URL https://doi.org/10.1007/BF01339504.

[4] Chan, C.-K., Lindner, N. H., Refael, G. & Lee, P. A. Photocurrents in weyl semimetals. *Phys. Rev. B* **95**, 041104 (2017). URL https://link.aps.org/doi/10.1103/PhysRevB.95.041104.

[5] Li, H. *et al.* Negative magnetoresistance in dirac semimetal cd3as2. *Nature Communications* **7**, 10301 (2016). URL https://doi.org/10.1038/ncomms10301.

[6] Kutayiah, A. R. *Nonlocal Nonlinear Optics in Graphene and the Optics of Weyl Semimetals.* Ph.D. thesis, Texas AM University (2019).

[7] Hosur, P. & Qi, X. Recent developments in transport phenomena in weyl semimetals. *Comptes Rendus Physique* **14**, 857 – 870 (2013). URL http://www.sciencedirect.com/science/article/pii/S1631070513001710. Topological insulators / Isolants topologiques.

[8] Girvin, S. M. & Yang, K. *Modern Condensed Matter Physics* (Cambridge University Press, 2019).

[9] Lv, B. Q. *et al.* Observation of weyl nodes in taas. *Nature Physics* **11**, 724–727 (2015). URL https://doi.org/10.1038/nphys3426.

[10] Xu, S.-Y. *et al.* Discovery of a weyl fermion semimetal and topological fermi arcs. *Science* **349**, 613–617 (2015). URL https://science.sciencemag.org/content/349/6248/613. https://science.sciencemag.org/content/349/6248/613.full.pdf.

[11] Morimoto, T. & Nagaosa, N. Topological nature of nonlinear optical effects in solids. *Science Advances* **2** (2016). URL https://advances.sciencemag.org/content/2/5/e1501524. https://advances.sciencemag.org/content/2/5/e1501524.full.pdf.

[12] Boyd, R. W. *Nonlinear Optics* (Academic Press, 2003), 2nd ed edn.

[13] Jauho, A.-P., Wingreen, N. S. & Meir, Y. Time-dependent transport in interacting and noninteracting resonant-tunneling systems. *Phys. Rev. B* **50**, 5528–5544 (1994). URL https://link.aps.org/doi/10.1103/PhysRevB.50.5528.

[14] Oka, T. & Aoki, H. Photovoltaic hall effect in graphene. *Phys. Rev. B* **79**, 081406 (2009). URL https://link.aps.org/doi/10.1103/PhysRevB.79.081406.

[15] Armitage, N. P., Mele, E. J. & Vishwanath, A. Weyl and dirac semimetals in three-dimensional solids. *Rev. Mod. Phys.* **90**, 015001 (2018). URL https://link.aps.org/doi/10.

1103/RevModPhys.90.015001.

[16] Hosur, P., Parameswaran, S. A. & Vishwanath, A. Charge transport in weyl semimetals. *Phys. Rev. Lett.* **108**, 046602 (2012). URL https://link.aps.org/doi/10.1103/PhysRevLett.108.046602.

[17] Kobayashi, K., Ohtsuki, T., Imura, K.-I. & Herbut, I. F. Density of states scaling at the semimetal to metal transition in three dimensional topological insulators. *Phys. Rev. Lett.* **112**, 016402 (2014). URL https://link.aps.org/doi/10.1103/PhysRevLett.112.016402.
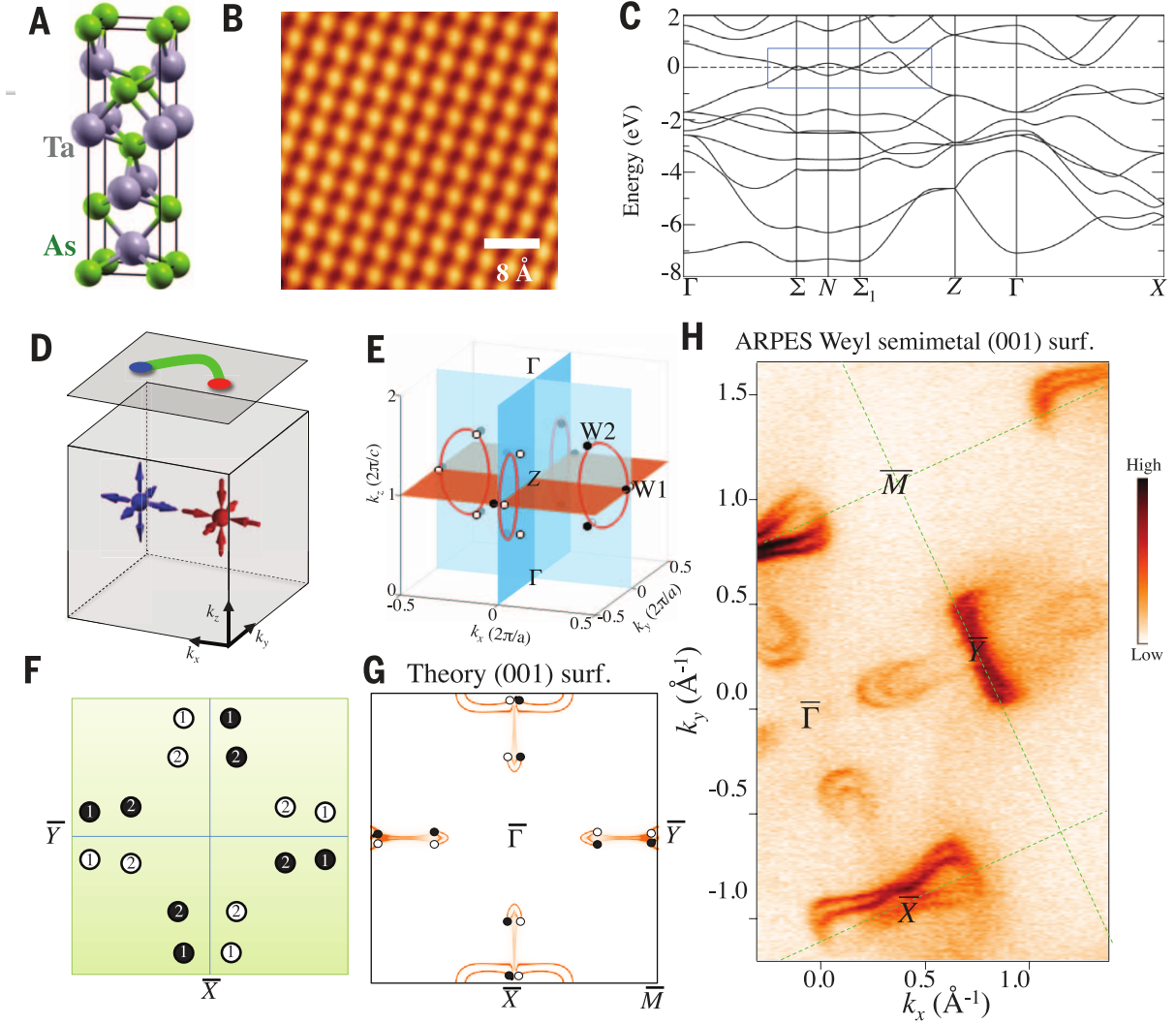
A.   Additional Figures

FIG. S1. (a) structure of TaAs (b) STM topographic image of TaAs's (001) surface (c) First-principles band structure calculations of TaAs (d) Illustration of the simplest Weyl semimetal state that has two single Weyl nodes with the opposite chirality (e) 24 Weyl nodes in the bulk of TaAs (f)A schematic diagram showing the projected Weyl nodes and their projected chiralities (g) theoretical prediction of Fermi surface on the (001) surface of TaAs (h)The ARPES- measured Fermi surface of the (001) cleaving plane of TaAs [10]
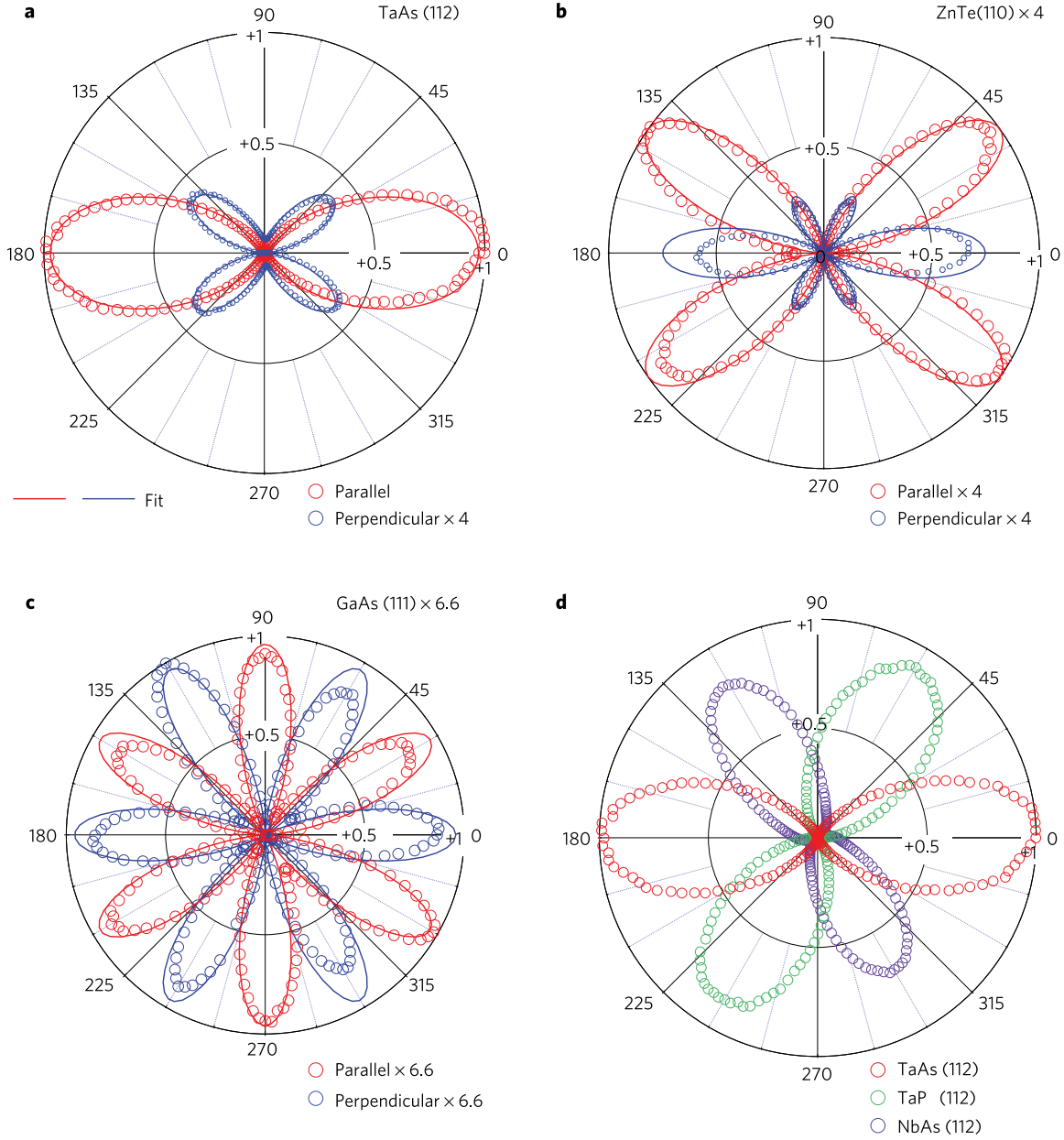
FIG. S2. Benchmark SHG experiments on TaAs (112), TaP (112), NbAs (112), ZnTe (110) and GaAs (111) [1]

B. Floquet Formalism

This formalism is the appropriate vehicle to study strongly driven periodic quantum systems, whose Hamiltonian is time-dependent subject to a periodic perturbation with period

T:

$$H(t) = H(t + T) \tag{S1}$$

For simplicity we start from the 1D Schrodinger equation:

$$\left(H(x, t) - i\hbar\frac{\partial}{\partial t} \right) \psi(x, t) = 0 \tag{S2}$$

with the total Hamiltonin dressed by a periodic perturbation $V(x, t) = V(x, t+T)$ such that $H(x, t) = H_0(x) + V(x, t)$. According to Floquet theorem, the solution takes on the form:

$$\psi_\alpha(x, t) = \exp(-i\epsilon_\alpha t/\hbar)\phi_\alpha(x, t) \tag{S3}$$

where $\phi_\alpha(x, t)$ is periodic in time, i.e. $\phi_\alpha(x, t) = \phi_\alpha(x, t+T)$. The exponent ϵ_α, being a real number, is termed quasienergy as an analogy with the quasimomentum in Bloch eigenstates. Note that ϵ_α is unique only upto multiples of $2\pi\hbar/T \equiv \hbar\omega$, the eigenvalues $\{\epsilon_\alpha\}$ can therefore be confined into the 1st Brillouin zone, i.e. $-\hbar\omega/2 \leq \epsilon_\alpha \leq \hbar\omega/2$. With Eq.(S2) and Eq.(S3), we get the eigenvalue equation for ϵ_α:

$$\mathcal{H}(x, t)\phi_\alpha(x, t) = \epsilon_\alpha\phi_\alpha(x, t), \quad \text{with} \ \ \mathcal{H}(x, t) \equiv H(x, t) - i\hbar\frac{\partial}{\partial t} \tag{S4}$$

It is readily to see that the Floquet modes can be defined by:

$$\phi_{\alpha n}(x, t) = \phi_\alpha(x, t)e^{in\omega t} \tag{S5}$$

with n being an integer $n = \pm 1, \pm 2, \dots$. As can be verified immediately by plugging into the eigen equation Eq.(S2):

$$\left(H(x, t) - i\hbar\frac{\partial}{\partial t} \right) \phi_{\alpha n} = (\epsilon_\alpha + n\hbar\omega)\phi_{\alpha n} \tag{S6}$$

the new Floquet mode $\phi_{\alpha n}$ has quasienergy shift by $\epsilon_\alpha \rightarrow \epsilon_{\alpha n} = \epsilon_\alpha + n\hbar\omega$, that is, the quasienergy ϵ is quantized by energy quanta of periodic perturbation. For the time-dependent $\mathcal{H}(x, t)$, it is convenient to work in the composite Hilbert space $\mathcal{R} \otimes \mathcal{T}$, i.e. a composite of space and time, since, from Eq.(S5) we notice that the temporal and spacial parts of Floquet states can be separated (from $t = 0$ and evolve by multiples of $e^{in\omega t}$). The inner product of $\mathcal{R}$ is:

$$\langle \eta_\alpha | \eta_\beta \rangle = \int dx \ \eta_\alpha^*(x)\eta_\beta(x) = \delta_{\alpha,\beta} \tag{S7}$$

26

and the innerproduct in $\mathcal{T}$:

$$\langle m|n \rangle = \frac{1}{T} \int_0^T dt \ \exp[i(n-m)\omega t] = \delta_{n,m} \tag{S8}$$

where we defined $\langle t|m \rangle \equiv \exp\{im\omega t\}$. Thus eigenvectors in $\mathcal{H}$ in composite Hilbert space $\mathcal{R} \otimes \mathcal{T}$ satisfies:

$$\langle \phi_{\alpha,m}|\phi_{\beta,n} \rangle = \frac{1}{T} \int_0^T dt \int dx \ \phi_{\alpha,m}^*(x,t)\phi_{\beta,n}(x,t) = \delta_{\alpha,\beta}\delta_{m,n} \tag{S9}$$

which forms a complete set in $\mathcal{R} \otimes \mathcal{T}$.

Now we are ready to move onto the application in band theory. Consider a Floquet state in Fourier space: $|\phi_\alpha(t)\rangle = \sum_m \exp\{-im\Omega t\}|u_\alpha^m\rangle$ with m being the label Floquet modes. The normalization gives:

$$\langle \phi_\alpha(t)|\phi_\alpha(t) \rangle = \sum_{m,n} e^{-i(m-n)\omega t} \langle u_\alpha^m|u_\alpha^n \rangle = \sum_m \langle u_\alpha^m|u_\alpha^m \rangle = 1 \tag{S10}$$

where we have used the orthogonality of Fourier modes. Since $H(t)$ breaks the continous time symmetry, the energy is not conserved. We thus ask the question: what role does Floquet modes play in energy. To answer this question, we look at the time-averaged energy $\bar{E}$ of a Floquet state $|\psi_\alpha(t)\rangle$:

$$\bar{E}_\alpha = \frac{1}{T} \int_0^T dt \ \langle \psi_\alpha(t)|H(t)|\psi_\alpha(t) \rangle = \epsilon_\alpha + \langle \phi_\alpha|i\hbar \frac{\partial}{\partial t}|\phi_\alpha \rangle \tag{S11}$$

note that $H(t)$ in evaluation is not Floquet operator but the Hamiltonian. Plug in Floquet modes by Fourier expansion and recall the orthoganality between different modes, we have:

$$\bar{E}_\alpha = \sum_n (\epsilon_\alpha + n\hbar\omega) \langle u_\alpha^n|u_\alpha^n \rangle \tag{S12}$$

Therefore the time-averaged energy $\bar{E}_\alpha$ can be viewed as the weighted sum of all Floquet modes of $\phi_\alpha(t)$.

Next we discuss qualitative, general features of quasienergies and Floquet modes with respect to their frequency and field dependence. By Eq.(S5) we know $|\phi_{\alpha 0}\rangle = |\phi_{\alpha n}\rangle e^{-i\omega nt}$, with $|\phi_{\alpha n}\rangle$ having quasienergy $\epsilon_{\alpha n} = \epsilon_{\alpha 0} + n\hbar\omega$. Hence we can identify the equivalence of two Floquet states:

$$|\psi_{\alpha 0}(t)\rangle = e^{-i\epsilon_{\alpha 0}t/\hbar} |\phi_{\alpha 0}(t)\rangle = e^{-i(\epsilon_{\alpha 0}+n\hbar\omega)t} |\phi_{\alpha k}\rangle = |\psi_{\alpha k}(t)\rangle \tag{S13}$$

C. Chern Number

Here I present the relation between a non-zero Chern number and Broken Time-Reversal Symmetry. Non-zero Chern number requires the breaking of time-reversal symmetry. The Chern number is defined as:

$$\mathcal{C} = \frac{1}{2\pi} \int_{1^{st}B.L.} d^2\vec{k}\, \Omega_z(\vec{k}) \tag{S14}$$

recall that the velocity with a generic Berry curvature is:

$$\vec{v} = \frac{1}{\hbar}\nabla_{\vec{k}}\epsilon_{\vec{k}} + \frac{e}{\hbar}\vec{E}\cdot\vec{\Omega}(\vec{k}) \tag{S15}$$

under time-reversal transformation we have $\dot{\vec{r}} \to -\dot{\vec{r}}, \dot{\vec{k}} \to -\dot{\vec{k}}, \vec{E} \to \vec{E}, \vec{B} \to -\vec{B}$, so we must have $\vec{\Omega}(\vec{k}) \to -\vec{\Omega}(-\vec{k})$. Therefore the Chern number changes by:

$$\mathcal{C} \to \mathcal{C} = -\frac{1}{2\pi}\int_{1^{st}B.L.} d^2\vec{k}\, \Omega_z(-\vec{k}) = -\frac{1}{2\pi}\int_{1^{st}B.L.} d^2\vec{k}'\, \Omega_z(\vec{k}') \tag{S16}$$

where in the last step we relabelled the dummy variable $\vec{k} \to \vec{k}'$. Comparing with with Eq.(S14) we conclude:

$$\mathcal{C} \xrightarrow{\mathcal{T}} -\mathcal{C} \tag{S17}$$

If the system respects $\mathcal{T}$ then we must have $\mathcal{C} = -\mathcal{C} \Rightarrow \mathcal{C} = 0$. Therefore in order to have a non-zero Chern number, the time-reversal symmetry must be broken.

D. Green's Functions

Green functions (or correlation) play a fundamental role in statistical physics since they constitute the connection between experimentally relevant quantities and conveniently calculable quantities. In a generic Fermi system (may be out of equilibrium), the distribution function $f(\epsilon)$ may no longer be the canonical distribution. Hence in addition to the retarded and advanced Green functions, we need correlation functions in spacetime, i.e. the greater and lesser Green function (of a Fermi field) defined by:

$$\begin{aligned}
G^>(\vec{x}_1,t_1;\vec{x}_2,t_2) &= -i\left\langle \psi(\vec{x}_1,t_1)\psi^\dagger(\vec{x}_2,t_2)\right\rangle \\
G^<(\vec{x}_1,t_1;\vec{x}_2,t_2) &= +i\left\langle \psi^\dagger(\vec{x}_2,t_2)\psi(\vec{x}_1,t_1)\right\rangle
\end{aligned} \tag{S18}$$

by which we can define the retarded and advanced Green function as

$$G^R(\vec{x}_1,t_1;\vec{x}_2,t_2) = +\mathcal{T}(t_1-t_2)\left[G^>(\vec{x}_1,t_1;\vec{x}_2,t_2) - G^<(\vec{x}_1,t_1;\vec{x}_2,t_2)\right] \tag{S19}$$

$$G^A(\vec{x}_1, t_1; \vec{x}_2, t_2) = -\mathcal{T}(t_2 - t_1)\left[G^>(\vec{x}_1, t_1; \vec{x}_2, t_2) - G^<(\vec{x}_1, t_1; \vec{x}_2, t_2)\right] \qquad \text{(S20)}$$

and time-ordered Green function $G^{\mathcal{T}}$ as:

$$
\begin{aligned}
G^{\mathcal{T}}(\vec{x}_1, t_1; \vec{x}_2, t_2) &= -i\left\langle \mathcal{T}\psi(\vec{x}_1, t_1)\psi^\dagger(\vec{x}_2, t_2)\right\rangle \\
&= -i\mathcal{T}(t_1 - t_2)\left\langle \psi(\vec{x}_1, t_1)\psi^\dagger(\vec{x}_2, t_2)\right\rangle + i\mathcal{T}(t_2 - t_1)\left\langle \psi^\dagger(\vec{x}_2, t_2)\psi(\vec{x}_1, t_1)\right\rangle \\
&= \mathcal{T}(t_1 - t_2)G^>(\vec{x}_1, t_1; \vec{x}_2, t_2) + \mathcal{T}(t_2 - t_1)G^<(\vec{x}_1, t_1; \vec{x}_2, t_2)
\end{aligned}
$$
$$\text{(S21)}$$

In an equilibrium system where the time-translational symmetry is respected, these functions depend only on the distance in time, i.e. $t = t_1 - t_2$. Hence we can rewrite a generic Green function into Fourier space by $G(\omega) = \int \exp(i\omega t)G(t)dt$. By Kubo–Martin–Schwinger condition, greater and lesser Green functions are related by $G^>(\omega) = -e^{\beta\omega}G^<(\omega)$, and spectral function $A(\omega) = i[G^>(\omega) - G^<(\omega)]$, hence

$$G^<(\omega) = if(\omega)A(\omega), \quad G^> = -i(1 - f(\omega))A(\omega) \qquad \text{(S22)}$$

where $f(\omega)$ is the Fermi-Dirac distribution. This distribution of $f(\omega)$, however, is only exact for equilibrium system, and need to be modified for the non-equilibrium systems.

1. Perturbation theory for equilibrium Green functions

Consider a Hamiltonian with interaction: $H = H_0 + V$ where H_0 describes the non-interacting part of the system. In interaction picture the wavefunction is definde by $|\psi_I(t)\rangle = \exp\{iH_0 t\}\exp\{-iHt\}|\psi(0)\rangle$. Field operator and S-matrix are defined by

$$\hat{\psi}_I(t) = e^{iH_0 t}\hat{\psi}e^{-iH_0 t}, \quad S(t, t_0) = \mathcal{T}\exp\left[-i\int_{t_0}^{t}V(t')dt'\right] \qquad \text{(S23)}$$

and time-depent operators in interaction picture is related to those in Heisenberg picture by:

$$\hat{\psi}_I(t) = S(t, t_0)\hat{\psi}(t)S(t_0, t), \quad \hat{\psi}(t) = S(t_0, t)\hat{\psi}_I(t)S(t, t_0) \qquad \text{(S24)}$$

Thus we immediately obtain:

$$\left\langle \psi(t_1)\psi^\dagger(t_2)\right\rangle = \left\langle e^{iH_0 t_0}S(t_0, t_1)\psi_I(t_1)S(t_1, t_2)\psi_I^\dagger(t_2)S(t_2, t_0)e^{-iH_0 t_0}\right\rangle \qquad \text{(S25)}$$

where the wavefunction and operators on LHS are represented in Heisenberg picture, while on RHS they are in interaction representation, with the exponential at the two ends being

the compensation factor for swithing from Heisenberg ket to interaction ket. This can be interpreted as the following: start from t_0, evolve the system till t_2 at which the creation operator is applied. Hereafter the system is evolved to t_1 at which the annihilation operator is applied, then evolve backward to the starting point t_0. It readily to notice that such a procedure can be written compactly by

$$\langle \psi(t_1)\psi^\dagger(t_2)\rangle = \left\langle e^{iH_0t_0}\mathcal{T}_\mathcal{C}S_\mathcal{C}\psi_I(t_1)\psi_I^\dagger(t_2)e^{-iH_0t_0}\right\rangle \tag{S26}$$

$$S_\mathcal{C} = \mathcal{T}\exp\left[-i\int_\mathcal{C}V_I(\tau)d\tau\right] \tag{S27}$$

where $\mathcal{T}_\mathcal{C}$ is the time-order operator on the closed contour of time $\mathcal{C}$. In order to use the canonical ensemble in the unperturbed H_0, we are tempted to expand the statistical operator $\exp\{-\beta H\}$ such that the Boltzmann factor $\exp\{-\beta H_0\}$ can be separated out.

$$\exp\{-\beta H\} = \underbrace{\left(e^{-iH_0(t_0-i\beta)}e^{iH_0(t_0-i\beta)}\right)}_{\mathbb{1}}\underbrace{\left(e^{-iH(t_0-i\beta)}e^{iHt_0}\right)}_{\exp\{-\beta H\}}\underbrace{\left(e^{-iH_0t_0}e^{iH_0t_0}\right)}_{\mathbb{1}}$$

$$= e^{-iH_0(t_0-i\beta)}\underbrace{\left(e^{iH_0(t_0-i\beta)}e^{-iH(t_0-i\beta)}\right)}_{U(t_0-i\beta)}\underbrace{\left(e^{iHt_0}e^{-iH_0t_0}\right)}_{U^\dagger(t_0)}e^{iH_0t_0} \tag{S28}$$

$$= e^{-iH_0(t_0-i\beta)}S(t_0-i\beta,t_0)e^{iH_0t_0}$$

Then the correlation becomes

$$\langle\psi(t_1)\psi^\dagger(t_2)\rangle = \left\langle\mathcal{T}_{\mathcal{C}'}S_{\mathcal{C}'}\psi_I(t_1)\psi_I^\dagger(t_2)\right\rangle_0 \Big/ \langle\mathcal{T}_{\mathcal{C}'}S_{\mathcal{C}'}\rangle_0 \tag{S29}$$

2. Keldysh Green's Function

The Keldysh Green's function in the Floquet formalism is given by Dyson equation in [14].

$$\begin{pmatrix} G^R & G^K \\ 0 & G^A \end{pmatrix}_{mn}^{-1} = \begin{pmatrix} (\omega+n\omega)\delta_{mn}-H_{mn} & 0 \\ 0 & (\omega+n\omega)\delta_{mn}-H_{mn} \end{pmatrix} + \Sigma_{mn} \tag{S30}$$

where H_{mn} is the unperturbed Hamiltonian H_0 expanded in Floquet modes, m,n are indices of Floquet modes, and Σ_{mn} is the self-energy given by

$$\Sigma_{mn} = i\Gamma\delta_{mn}\begin{pmatrix} \frac{1}{2} & -1+2f(\omega+m\Omega) \\ 0 & -\frac{1}{2} \end{pmatrix} \tag{S31}$$

30

where we have assumed that the system is coupled to a heat reservoir with the Fermi distribution $f(\epsilon)$ with a coupling constant Γ. Then the current is generally given by

$$J(t) = \sum_m -i \operatorname{Tr}[v(t)G^<_{mn}]e^{-i(m-n)\Omega t} \tag{S32}$$

We don't have to calculate the lesser Green's function $G^<$ from scratch, but it can be given by the Keldysh equation [13]

$$G^< = G^R \Sigma^< G^A, \quad \text{with} \quad \Sigma^< = \frac{\Sigma^R + \Sigma^K - \Sigma^A}{2} \tag{S33}$$

we can get the retarded and advanced Green's function directly from Eq.(S30), that is

$$(G^{R/A})^{-1}_{mn} = \left(\omega + n\Omega \pm \frac{i\Gamma}{2}\right)\delta_{mn} - H_{mn} \tag{S34}$$

Hence the DC current reads

$$J = \sum_m -i \operatorname{Tr}[\tilde{v}_{nm}G^<_{mn}] \tag{S35}$$

with $\tilde{v} = \partial H_F/\partial k$.